Parametric instability in the formation of plasma waveguides

J. H. Cooley

Los Alamos National Laboratory, Los Alamos, New Mexico 87545, USA

T. M. Antonsen

Institute for Research in Electronics and Applied Physics, University of Maryland, College Park, Maryland 20742, USA

H. M. Milchberg and J. Fan

Institute for Physical Science and Technology, University of Maryland, College Park, Maryland 20742, USA

L. Margolin* and L. Pyatnitskii

Institute for High Temperatures, Russian Academy of Sciences, Moscow, Russia

Plasma waveguides generated by focusing a moderate intensity laser into neutral gas with an axicon lens can be unstable to the generation of axial modulations in the channel parameters. A model is proposed in which the modulations are due to the nonlinear coupling between the axicon field and a scattered mode in the evolving channel. Good agreement is found with experimental measurements of these modulations.

PACS number(s): 52.38.Dx, 52.35.Mw

I. INTRODUCTION

Plasma waveguides for guiding intense laser pulses have applications in particle accelerators and x-ray generation schemes [1,2]. Waveguides can be formed using a variety of methods [3–6]. One method is to create a plasma channel by ionizing a gas with a moderate intensity laser pulse focused through an axicon. The axicon focuses the laser pulse to a line where gas is ionized and expands, creating a shock, and leaving an electron density profile with an off-axis maximum that defines the channel. Ideally, the plasma channel will be axially symmetric and allow for guiding of high-intensity light over distances of many Rayleigh lengths, $Z_r = \pi w^2 / \lambda$, where w is the vacuum focal spot size and λ is the laser wavelength. Axially symmetric channels have been produced using axicon focusing of $\sim$100 ps laser pulses in low-pressure gas, and their evolution is well understood [7–9]. However, as the gas pressure is raised, the plasma channel affects the propagation of the axicon pulse and new and interesting phenomena occur. For example, at specific values of initial gas pressure the axicon field couples strongly to guided modes in the resulting plasma channel and linear resonant absorption occurs [9]. This linear absorption still yields axially smooth channels. As pressure is increased further, axial modulations with definite periodicity begin to appear on a time scale comparable to the $\sim$100 ps laser pulse. This is distinct from previous observations [10–12] of axial modulations at even higher pressures and at pulse durations significantly longer than a typical channel expansion time scale [3] of $w/c_s \sim 1$ ns, where w is the laser spot size and c_s is the plasma sound speed. In those experiments, modulations appear due to interference between the incoming and outgoing rays of the heating pulse. In this paper we present evidence of axial modulations that occur at intermediate pressures and on much faster time scales and argue that these modulations result from a distinct form of nonlinear resonant absorption that has the character of a parametric instability. Further, we present a model of this instability and describe the growth of the unstable perturbations.

In the experiment, a 100 ps (FWHM) laser pulse of wavelength 1.064 μm was focused through an axicon lens into uniform ambient argon gas of variable pressure, with a peak vacuum intensity of 5×10^{13} W/cm^2. Axicons with base angles from 10° to 30° were used. However, the axial modulation results varied weakly with the axicon angle, and the results presented below are for the 25° base angle axicon. A delayed probe pulse, split from the main pulse, is incident perpendicular to the axis of the evolving channel and imaged into a charge coupled device (CCD) camera. The probe pulse can be imaged directly into the camera, generating a shadowgram, or it can be passed through a glass wedge, generating an interferogram. When the channel is azimuthally symmetric the interferograms have been used to deduce time evolving radial profiles of electron density [7,8]. These profiles compare well with those predicted from a one-dimensional hydrodynamic code [9] that we will use in this work.

Figure 1 shows a set of shadowgrams taken for a series of background pressures of argon: (a) 200 torr, (b) 280 torr, (c) 300 torr, (d) 340 torr, (e) 370 torr, and (f) 420 torr taken at a pump-probe delay of 330 ps. The figure shows an 0.8 mm axial section of the channels. The total length of the channel is about 15 mm. The channel is seen to be relatively axially uniform on the scale of the image for pressures 300 torr and less. This is not the case for the channels formed in higher pressure, 340 torr and greater. Here a distinct axial modulation of the channel is evident. The density variations in the highest-pressure case are of the order of 10% based on interferograms. The wavelength of the modulation, calculated by Fourier transforming the image intensity along the axis of the

---

*Deceased.
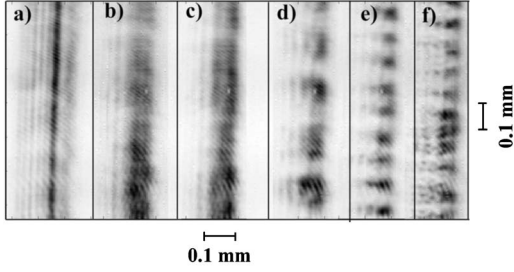
FIG. 1. Shadowgrams of channels formed in argon for different pressures: (a) 200 torr, (b) 280 torr, (c) 300 torr, (d) 340 torr, (e) 370 torr, and (f) 420 torr. Laser pulse: 100 ps FWHM, λ =1064 nm, and peak intensity 5×10^{13} W/cm²; and axicon base angle 25°.

channel and finding the wave number peaks, is approximately 0.14 mm and 0.09 mm in the 340 and 370 torr cases, respectively. Note that there is a relatively large change in wavelength that accompanies a relatively small increase in pressure. Our model of the modulations explains this observation.

According to our explanation, the modulations are the result of a nonlinear absorption process that involves a coupling between the incident axicon field, a guided mode of the channel, and the axial modulations of the channel parameters. Specifically, the axicon focuses the formation pulse rays at an angle θ to the axis of the axicon, which we take to be the z axis (cos θ=0.967 in the experiment). Thus, the axicon field has an axial wave number $k_a=k_0\sqrt{1+4\pi\chi}$ cos θ, where $k_0=\omega_0/c$ is the laser vacuum wave number and χ is the susceptibility of the gas (for argon under the conditions of the experiment, $4\pi\chi=1.36\times10^{-4}$, for P=200 torr). The axicon creates a plasma channel that after time can support guided modes with axial wave number k_g, which is a function of the channel density profile as well as the azimuthal and radial mode indices of the mode in question [8]. Linear resonance absorption [9] occurs when the axicon and guided mode wave numbers match, $k_a=k_g$. In this case the axicon field can tunnel through the wall of the channel and excite a quasi-guided mode. This occurs at specific values of initial gas density and time for a given mode. Nonlinear absorption occurs as the result of a parametric instability. If there is a small axial modulation of the channel parameters with wave number $k_m=k_g-k_a\neq0$, then the axicon field will be scattered into the guided mode. The local heating rate in the channel, which is proportional to the laser intensity, will then have an axial modulation at k_m due to the beating of the axicon field and the guided mode. This modulated heating rate will reinforce the initially small modulation of channel parameters and result in exponential growth of the channel modulations and increased absorption of the axicon field. The previously mentioned insensitivity of the modulation wave number to axicon base angle follows from the fact that for small angles cos $\theta\approx1$, and consequently k_m is a weak function of θ.

The organization of the remainder of this paper is as follows. In Sec. II we develop a linear theory for the formation of modulations in an expanding channel based on fluid equations. This leads to an eigenvalue equation for the growth rate of perturbations with a specified axial wave number. We

then give an approximate analytical solution to this eigenvalue problem in the case in which the channel is deep. We also discuss the space-time evolution of perturbations and show that the instability is absolute in the lab frame. In Sec. III we present numerical solutions for the growth rate of the modulations based on channel profiles that are predicted by the hydro-code. We then integrate the growth rate over time during the formation of a channel to arrive at a value of the cumulative growth of the instability as a function of modulation wave number. We then compare this prediction with the images in Fig. 1. In Sec. IV we present a modified model to examine the effect of high electron thermal conductivity and assess the importance of thermal relaxation on the instability growth. In Sec. V we discuss and summarize our results.

II. LINEAR THEORY OF MODULATION GROWTH

To lend support to our picture of the development of modulations we investigate the linear stability of the formation of an axially symmetric channel to perturbations with axial modulations. In our model, the electric field consists of a symmetric axicon pulse $\boldsymbol{E}_a$ and a small, scattered wave, $\widetilde{\boldsymbol{E}}_s$,

$$\boldsymbol{E}(r,t) = \text{Re}\{\boldsymbol{E}_a(r)\exp[i(k_a z - \omega_0 t)]$$
$$+ \widetilde{\boldsymbol{E}}_s(r,z,t)\exp[i(k_s z + m\theta - \omega_0 t)]\}. \quad (1)$$

Similarly, the electron density is written as the sum of a symmetric part and a small perturbation with modulations,

$$n_e(\boldsymbol{r},t) = n_0(r) + \text{Re}[\widetilde{n}(r,t)\exp(ik_m z + im\theta)], \quad (2)$$

where $k_m=k_s-k_a$. The axicon field amplitude, which we assume to be linearly polarized, satisfies a radial differential equation of the form

$$[\nabla_\perp^2 + \kappa^2(r,\omega_0,k_a)]E_a(r) = 0, \quad (3)$$

where $\kappa^2=k_0^2(1+4\pi\chi)-k_a^2-4\pi r_e n_0(r)(1+i\nu/\omega_0)^{-1}$ [9], ν is the electron-ion collision rate, and r_e is the classical electron radius. The amplitude of the incoming axicon wave at $r \to \infty$ is specified. The electron density profile, $n_0(r)$, is determined self-consistently along with the amplitude of the axicon field, $\boldsymbol{E}_a$, by the previously mentioned one-dimensional hydrodynamic code [9] that includes the relevant formation processes such as ionization, Joule heating, and thermal conduction. The beating of the axicon field and the density modulations drives the scattered wave,

$$\left(\nabla_\perp^2 + 2i\frac{\omega_0}{c^2}\frac{\partial}{\partial t} + \kappa^2(r,\omega_0,k_s)\right)\widetilde{E}_s(r,t) = 4\pi r_e\widetilde{n}_e(r,t)E_a,$$
$$(4)$$

where the scattered wave is polarized in the same direction as the axicon field.

The density perturbation is determined by the linearized equations of continuity, momentum balance, and energy balance,

$$\frac{\partial}{\partial t}\tilde{n} + \boldsymbol{\nabla} \cdot \tilde{\nu} n_0(r) = 2n_0 \tilde{n} S(T_e) + n_0^2 \tilde{T}_e \frac{\partial S}{\partial T_e}$$

$$+ n_0(\tilde{n}_s T_a^* + n_a^* \tilde{T}_s)\frac{\partial S}{\partial T_e}, \quad (5\text{a})$$

$$m_i n_0(r)\frac{\partial}{\partial t}\tilde{\nu}(r,t) = -\boldsymbol{\nabla}_\perp \tilde{p} - \frac{1}{2}\frac{n_0 e^2}{m_e c^2}\boldsymbol{\nabla}_\perp[\tilde{E}_s(r,t)E_a^*], \quad (5\text{b})$$

$$\frac{3}{2}\frac{\partial}{\partial t}\tilde{p} = \frac{n_0 e^2}{m_e}\frac{\nu}{\nu^2 + \omega_0^2}\tilde{E}_s(r,t)E_a^*. \quad (5\text{c})$$

Here we have neglected convective terms on the left-hand side of the fluid equations under the simplifying assumption that the growth time is less than the channel evolution time. By the same reasoning, we neglect perturbations in the heating rate due to perturbations in density and temperature. We also have neglected thermal conduction in the present model. We will assess the effects of thermal relaxation in Sec. IV.

The terms on the right-hand side of Eq. (5a) represent the linearization of the collisional ionization rate, $n^2 S(T_e)$ where $S = \Sigma_i S_i(T_e) n_i/n$, $nn_i S_i(T_e)$ is the rate of collisional ionization of the ith ionized stage of the working gas, and $S_i(T_e)$ is given by $S_i(T_e) = 9 \times 10^{-6}\sqrt{T_e/U_i}\exp(-U_i/T_e)/U_i^{3/2}(T_e/U_i + 4.88)$ [13], where U_i is the ionization potential for the ith electron, in eV. The first two terms in (5a) represent modifications to the ionization rate due to low-frequency perturbations in electron density and temperature. In the linearization of these terms we have assumed for simplicity that the ratios n_i/n remain fixed for low-frequency perturbations. This eliminates the need to follow the perturbations in the individual ionization stage densities. The last term represents the modification of the ionization rate due to the beating of high-frequency perturbation of the electron density and temperature. These perturbations arise if the electron quiver motion in the axicon field and the scattered field carries the electrons across temperature and density gradients. Specifically,

$$\frac{\tilde{n}_{a,s}}{n_0} = \frac{q\tilde{E}_{a,s} \cdot \boldsymbol{\nabla} n_0}{\omega(\omega + i\nu)mn_0},$$

and

$$\frac{\tilde{T}_{a,s}}{T_0} = \frac{q\tilde{E}_{a,s} \cdot \boldsymbol{\nabla} T_0}{\omega(\omega + i\nu)mT_0}.$$

Finally, we have neglected motion in the z direction under the assumption that the channel radius is much less than the axial wavelength of the modulations. This is well satisfied for pressures below 370 torr, but marginally satisfied at higher pressures.

On the right-hand side of Eqs. (5a)–(5c) we have three nonlinear terms allowing coupling of the scattered mode field to the density perturbation in the presence of the axicon field. These are the nonlinearly modified ionization rate in Eq. (5a), the ponderomotive force in Eq. (5b), and the Joule heating rate in (5c).

We assume perturbations grow exponentially in time with a complex growth rate γ. Thus, each of the perturbed quan-

tities in Eqs. (5) is expressed in terms of a complex amplitude and a time dependent exponential factor, viz. $\tilde{n} = \hat{n}\exp(\gamma t)$. We also assume the pressure satisfies the ideal gas law, $\hat{p} = n_0\hat{T} + \hat{n}T_0$. With these assumptions we can combine Eqs. (5) to obtain an expression for the complex amplitude of the density modulation,

$$\frac{\hat{n}}{n_0} = \frac{c^2}{\omega_p^2 \Delta}\left|\boldsymbol{\nabla}_\perp^2\left(\frac{\gamma_0^3}{\gamma^3}u_s u_a^*\right) + \boldsymbol{\nabla}_\perp \cdot \left(\frac{\gamma_p^2}{\gamma^2}\boldsymbol{\nabla}_\perp u_s u_a^*\right)\right.$$

$$\left. + \frac{\omega_p^2}{c^2}\left(\frac{\gamma_I^2}{\gamma^2} + \frac{\gamma_s}{\gamma}\right)u_s u_a^*\right|, \quad (6)$$

where we have introduced the following notation. The quantity Δ in the denominator of (6) is given by

$$\Delta = 1 + \frac{\nu_I(\eta - 2)}{\gamma}, \quad (7)$$

where $\nu_I = n_0 S$ is the radially varying ionization rate and $\eta = d\ln S/d\ln T_e$. Other quantities in Eq. (6) are the growth rates

$$\gamma_0^3 = (2/3)k_p^2(m_e/m_i)\nu V_{osc}^2,$$

$$\gamma_p^2 = \gamma_0^3/(3\nu),$$

$$\gamma_I^2 = (2/3)\nu_I \eta(m_e/T_e)\nu V_{osc}^2,$$

and

$$\gamma_s = \nu_I \eta V_{osc}^2/(\omega^2 r_n r_T),$$

where $V_{osc}^2 = (e/m_e)^2|E_{a0}|^2/(\omega_0^2 + \nu^2)$ is the oscillation velocity based on the axicon field amplitude E_{a0}, $u_a(r) = E_a(r)/E_{a0}$ and $u_s(r) = E_s(r)/E_{a0}$ are the normalized axicon and scattered field profiles, and $r_{n,T}^{-1} = d\log(n,T)/dr$ are the inverse scale length for density or temperature. Terms involving γ_0 originate from the nonlinear perturbation of the heating rate in (5c). Terms involving γ_p originate from the ponderomotive force in (5b), and terms involving ν_I, γ_I, or γ_s originate from the perturbations of the ionization rate in (5a).

Equations (4) and (6) can be combined into an eigenvalue equation for the scattered field profile and growth rate,

$$\left[\boldsymbol{\nabla}_\perp^2 + 2i\frac{\omega_0}{c^2}\gamma + \kappa^2(r,\omega_0,k_s)\right]u_s$$

$$= \frac{u_a}{\Delta}\left[\boldsymbol{\nabla}_\perp^2\left(\frac{\gamma_0^3}{\gamma^3}u_s u_a^*\right) + \boldsymbol{\nabla}_\perp \cdot \left(\frac{\gamma_p^2}{\gamma^2}\boldsymbol{\nabla}_\perp u_s u_a^*\right)\right.$$

$$\left. + \frac{\omega_p^2}{c^2}\left(\frac{\gamma_I^2}{\gamma^2} + \frac{\gamma_s}{\gamma}\right)u_s u_a^*\right]. \quad (8)$$

This equation can in turn be put in the form of a second-order ordinary differential equation for the radial profile $\hat{u}_s(r)$, where $u_s(\mathbf{r}) = \hat{u}_s(r)\exp(im\theta)$,

$$M(r)\frac{d^2}{dr^2}\hat{u}_s + N(r)\frac{d}{rdr}\hat{u}_s + Q(r)\hat{u}_s = 0. \quad (9)$$

The coefficients in (9) are defined as

$$M(r) = 1 + \nu_I \frac{\eta - 2}{\gamma} - \frac{\omega_0 |u_a(r)|^2}{2(\omega_0 + i\nu)} \left(\frac{\gamma_0^3}{\gamma^3} + \frac{\gamma_p^2}{\gamma^2} \right), \quad (10a)$$

$$N(r) = 1 + \nu_I \frac{\eta - 2}{\gamma} - \frac{\omega_0 u_a}{2(\omega_0 + i\nu)} \left[\frac{rd}{dr} \left(\frac{\gamma_0^3}{\gamma^3} u_a^* \right) + \frac{d}{dr} \left(\frac{r\gamma_0^3}{\gamma^3} u_a^* \right) \right.$$

$$\left. + \frac{d}{dr} \left(\frac{r\gamma_p^2}{\gamma^2} u_a^* \right) + \frac{r\gamma_p^2}{\gamma^2} \frac{d}{dr} u_a^* \right], \quad (10b)$$

and

$$Q(r) = \left(1 + \nu_I \frac{2 - \eta}{\gamma} \right) \left(\kappa^2 - \frac{m^2}{r^2} \right) + \frac{\omega_0 |u_a|^2}{2(\omega_0 + i\nu)} \frac{\omega_p^2}{c^2} \frac{\gamma_I^2}{\gamma^2}$$

$$- \frac{\omega_0 u_a}{2(\omega_0 + i\nu)} \left[\frac{d}{rdr} \frac{rd}{dr} \left(\frac{\gamma_0^3}{\gamma^3} u_a^* \right) - \frac{m^2}{r^2} \left(\frac{\gamma_0^3}{\gamma^3} u_a^* \right) \right.$$

$$\left. + \frac{d}{rdr} \left(r \frac{\gamma_p^2}{\gamma^2} \frac{d}{dr} u_a^* \right) - \frac{m^2}{r^2} \left(\frac{\gamma_p^2}{\gamma^2} u_a^* \right) \right]. \quad (10c)$$

Equation (9) is to be solved for the eigenvalue $\gamma(k_s, t)$ (the growth rate) subject to the conditions that $\hat{u}_s$ is regular at the origin and corresponds to outgoing waves as $r \to \infty$. The eigenvalue γ depends parametrically on time and scattered wave number k_s. We will be interested in the cumulative growth $\Gamma(k_s) = \int dt \, \gamma(k_s, t)$ which determines the growth in perturbations with different modulation wave numbers $k_m = k_s - k_a$. The observed modulations are presumably the ones that correspond to the largest value of Γ. Numerical solutions of Eq. (9) will be presented in the next section. Here we will discuss qualitatively the types of solutions that can be found. First it is necessary to describe the physics of the channel formation. Figure 2 shows radial profiles of electron density, electron temperature, and ionization rate at three different times $t = 88$, 138, and 188 ps, during the formation of the channel. These are obtained from our one-dimensional hydro-code [9] and correspond to the illumination of 380 torr of argon by a 100 ps, 5×10^{13} W/cm^2 vacuum intensity 1.064 μm wavelength laser pulse. The basic process of channel formation is evidenced in Fig. 2(a) where the density profiles are shown. Initially the gas is broken down and the electron density peaks on axis. The electrons are collisionally heated to a temperature in the range of 70 eV as shown in Fig. 2(b), and thermal expansion begins to drive an outward propagating shock wave. By 90 ps the electron density profile has become inverted. At later times the channel broadens further and the temperature drops as electron thermal energy is used to drive the shock wave. The shock front is visible in Fig. 2(c) where the local ionization rate peaks. The example shown in Fig. 2 corresponds to a relatively high pressure for which the channel electron density is high enough to modify the axicon field profile. This is shown in Fig. 3 where the magnitude of the axicon field is plotted at the first two times shown in Fig. 2. As can be seen, early in the pulse the axicon field reaches the axis, while as the channel forms and expands the axicon field is excluded from the central region of the channel.

We now discuss the general features of the modes that are described by Eq. (9). The first type of mode is associated with the singular points of the equation where the coefficient
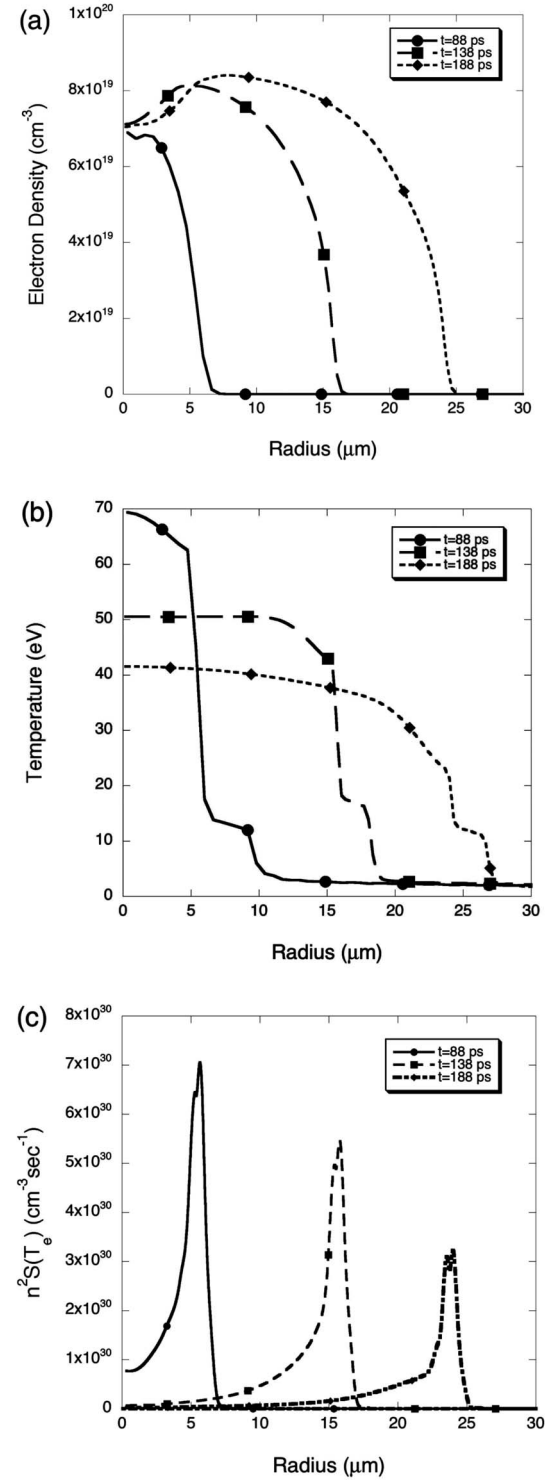
FIG. 2. Simulation results at three different times during the evolution from the 1D hydrodynamic code [9] for a simulation pressure of 380 torr argon and a laser pulse with peak intensity 5×10^{13} W/cm^2. The figures present the (a) electron plasma density, (b) electron temperature in electron volts, and (c) ionization rate given by $n^2 S(T_e)$. Notice that the channel is just starting to appear at 88 ps and that the interior parameters of this channel are relatively stable once formed. Also notice that the ionization front moves radially out as the channel expands.
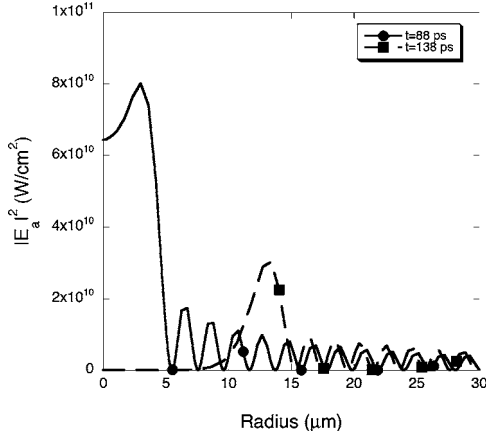
FIG. 3. Results of the self-consistent axicon field evolution as calculated with the 1D hydrodynamic code [9]. Notice that even by 88 ps when the channel has just started to form, the axicon field is beginning to be suppressed on the channel axis. This suppression is complete by 138 ps.

of the second derivative term vanishes, $M=0$. At any given radial point the condition $M=0$ defines a local dispersion relation that is cubic in growth rate. Two of the modes can be associated with the nonlinear beating of the scattered and axicon fields that act through the heating and ponderomotive force to produce density modulations. The third mode exists even in the absence of this beating and is given by $\gamma = \nu_I(2 - \eta)$. This mode, which we will refer to as the ionization mode, arises because of the strong dependence of the collisional ionization rate on electron density. Regions of space with elevated electron density have elevated ionization rates and in these regions the electron density grows even faster. The stabilizing term involving the logarithmic derivative with respect to temperature of the ionization rate results from the fact that, at fixed pressure, as the density goes up the temperature drops. During the course of the formation of the channel the local instantaneous ionization rate varies considerably as shown in Fig. 2(c). Initially the ionization rate is large on axis, but as the central region of the channel becomes ionized the local rate eventually drops. However, as the channel expands outward there is a region of ionization at the edge of the channel. We will find that there is usually an ionization mode that can be found somewhere in the channel.

The other two modes associated with the singular points $M=0$ are driven by the beating of the axicon and scattered fields. If we neglect the ionization rate, and consider these modes to act separately, they would have growth rates given by

$$\gamma^3 = \frac{\omega_0 |u_a(r)|^2}{2(\omega_0 + i\nu)} \gamma_0^3 \qquad (11a)$$

and

$$\gamma^2 = \frac{\omega_0 |u_a(r)|^2}{2(\omega_0 + i\nu)} \gamma_p^2. \qquad (11b)$$

Comparing these expressions, along with the definitions of γ_0 and γ_p, we see $\gamma_p^2 \approx \gamma_0^3/(3\nu)$. Thus, $\gamma_p < \gamma_0$ as long as

$\gamma_0 < \nu$, which turns out to be the case. Thus, the dominant nonlinearity is the modulated heating that results from the beating of the axicon and scattered wave fields.

A second basic type of mode is associated with the global solution of Eq. (9) rather than the local solution $M=0$. This mode is best understood as a weakly damped, quasi-bound mode of the channel that is coupled to the density perturbation through the axicon field. To analyze this mode we imagine that the scattered field profile is close to that of the guided mode, which satisfies

$$\left[\nabla_\perp^2 + 2i\frac{\omega_0}{c^2}(-\gamma_d) + \kappa^2(r, \omega_0, k_g) \right] u_g = 0, \qquad (12)$$

where k_g is the axial wave number of the guided mode and γ_d is the temporal damping rate of the guided mode due to the combination of energy leakage through the wall of the channel and collisional dissipation in the channel. The guided mode will have an axial wave number that is close to, but different from, the scattered wave number k_s, which at this point is a parameter to be specified. We obtain an approximate dispersion relation by inserting $\hat{u}_s \approx \hat{u}_g$ in Eq. (8), multiplying by $\hat{u}_g^*$ and integrating over radius,

$$2\frac{\omega_0}{c} \left| \frac{i}{c}(\gamma + \gamma_d) - (k_s - k_g) \right| \left| \int 2\pi r dr |u_g|^2 \right.$$

$$= \int 2\pi r dr \frac{u_a u_g^*}{\Delta} \left| \nabla_\perp^2 \left(\frac{\gamma_0^3}{\gamma^3} u_g u_a^* \right) + \nabla_\perp \cdot \left(\frac{\gamma_p^2}{\gamma^2} \nabla_\perp u_g u_a^* \right) \right.$$

$$\left. + \frac{\omega_p^2}{c^2} \left(\frac{\gamma_I^2}{\gamma^2} + \frac{\gamma_s}{\gamma} \right) u_g u_a^* \right|. \qquad (13)$$

If we assume the growth rate is larger than the ionization rate such that $\Delta \approx 1$, we may rewrite Eq. (13) as a fourth-order polynomial in γ,

$$\frac{2}{k_0} \left[\frac{i}{c}(\gamma + \gamma_d) - (k_s - k_g) \right] = \frac{A}{\gamma^3} + \frac{B}{\gamma^2} + \frac{C}{\gamma}, \qquad (14)$$

where

$$A = \frac{k_0^{-2} \int 2\pi r dr u_a u_g^* \nabla_\perp^2 (\gamma_0^3 u_g u_a^*)}{\int 2\pi r dr |u_g|^2}, \qquad (15a)$$

$$B = \frac{k_0^{-2} \int 2\pi r dr u_a u_g^* \left[\nabla_\perp \cdot (\gamma_p^2 \nabla_\perp u_g u_a^*) + \frac{\omega_p^2}{c^2} \gamma_I^2 u_g u_a^* \right]}{\int 2\pi r dr |u_g|^2}, \qquad (15b)$$

and

$$C = \frac{k_0^{-2} \int 2\pi r dr \frac{\omega_p^2}{c^2} \gamma_s |u_g u_a^*|^2}{\int 2\pi r dr |u_g|^2}. \tag{15c}$$

This dispersion relation (with $A = C = 0$) is closely related to that for the resonant instability of laser filaments in a plasma [14]. In the case of Ref. [14], a strong, self-guided, lowest-order mode of a ponderomotively created channel becomes unstable to the excitation of higher-order modes. In our case the axicon field replaces the strong, lowest-order mode and

the unstable perturbation is the lowest-order mode of the thermally created channel.

We anticipate that unstable modes will grow on the hydrodynamic time scale with wave number shifts on the order of the mode damping rate, $\delta k = k_s - k_g \approx k_d = \gamma_d/c$. This growth rate is much smaller than the temporal damping rate of a guided mode. Consequently we assume $\gamma \ll \gamma_d$ and drop γ on the left side of Eq. (14). Equation (14) is then a cubic polynomial. The most unstable growth rate will depend on the sizes of the coefficients A, B, and C. Roughly, we can say that the most unstable mode will satisfy

$$\gamma = \max \left\{ \mathrm{Re}\left[\left(\frac{k_0 A}{2(ik_d - \delta k)} \right)^{1/3} \right], \quad \mathrm{Re}\left[\left(\frac{k_0 B}{2(ik_d - \delta k)} \right)^{1/2} \right], \quad \mathrm{Re}\left[\left(\frac{k_0 C}{2(ik_d - \delta k)} \right) \right] \right\}.$$

Since the coefficients A, B, and C are all proportional to the axicon pulse intensity, as intensity is increased from zero the mode depending on A will have the largest growth rate because it scales with the lowest power of intensity. We thus set $B = C = 0$ and focus on this mode. In this case Eq. (14) can be recast,

$$D(\gamma, \delta k) = \gamma^3 + i \, \mathrm{sgn}(A)\Gamma_0^3/(1 + i\delta k/k_d) = 0, \tag{16}$$

where $\Gamma_0^3 = [|A|k_0/(2k_d)]$ is the nominal growth rate. Instability occurs for either sign of A. We estimate the magnitude of A from (15a) as

$$|A| \approx \frac{\gamma_0^2}{k_0^2 r_{ch}^2} = \frac{2}{3}\frac{\omega_p^2}{\omega_0^2}\tau_{heat}^{-1}\tau_{hydro}^{-2},$$

where $\tau_{heat}^{-1} = m_e \nu |V_{osc}|^2/T_e$ is the local heating rate and $\tau_{hydro}^{-2} = p_0/(n_0 m_i r_{ch}^2)$ is the hydrodynamic expansion rate where p_0 is the equilibrium pressure and r_{ch} is the channel radius. Based on this estimate, the nominal growth rate scales as $\Gamma_0 = [Q\omega_p^2 \tau_{heat}^{-1}\tau_{hydro}^{-2}/(3\omega_0^2)]^{1/3}$ where $Q = k_0/k_d$ represents the waveguide quality factor. Growth can occur on a time scale faster than the hydrodynamic time scale if the quality factor is large enough.

Using the dispersion relation (16) we can evaluate the space-time evolution of disturbances initiated at $z = 0$ at $t = 0$. This is done following the procedure outlined in Ref. [15]. Specifically we simultaneously solve $D(\gamma - i\delta k z/t, \delta k) = 0$ and $\partial D(\gamma - i\delta k z/t, \delta k)/\partial \delta k = 0$ to find γ and δk as functions of z/t. We then estimate the growth of the disturbance by evaluating $\mathrm{Re}(\gamma t + i\delta k z)$. We find the density perturbation grows as

$$|\hat{n}| \approx \exp[-k_d z + 2\cos(\pi/8)(\Gamma_0 t)^{3/4}(k_d z)^{1/4}].$$

Thus, for fixed axial location disturbances grow slower than exponentially. The rate of growth increases with axial distance. However, there is exponential damping with distance due to losses of the guided mode. If we maximize the growth over axial position we find the peak of the disturbance moves with constant speed,

$$k_d z_{peak} = \left(\frac{\cos(\pi/8)}{2} \right)^{4/3}\Gamma_0 t.$$

The amount of growth at this moving location is proportional to time,

$$|\hat{n}|_{peak} \approx \exp\left[3\left(\frac{\cos(\pi/8)}{2} \right)^{4/3}\Gamma_0 t \right].$$

Thus, the growth rate Γ_0 characterizes the instability. The main conclusion is that the instability is absolute in the lab frame, and the rate of growth can be estimated to be that which maximizes $\gamma(k_s)$.

III. NUMERICAL SOLUTIONS TO MODE EQUATIONS

Now we turn our attention to numerical solutions of Eq. (9). As was pointed out previously, we must solve Eq. (9) for the eigenvalue $\gamma(k_s)$, with requirements on the solution that it is regular at the origin and corresponds to outward propagating waves for larger radius. The coefficients M, N, and Q defined in (10) each depend on the unperturbed channel density and temperature distributions and the axicon field profile either directly or through differential operators. These distributions can be obtained using the 1D hydrodynamic code [9]. This hydrodynamic code provides self-consistent plasma densities and temperatures as well as the axicon fields at each 2.5 ps time interval during the formation of the plasma channel. The results of this code have been well characterized [9] and agree with experiment. Sample profiles are illustrated in Figs. 2(a)–2(c), for the plasma density, electron temperature, and ionization rate, and in Fig. 3, for the axicon electric field, for three different times during the formation of a channel.

To begin, we examine the eigenvalue and mode structure at one particular time, 88 ps, for a high-pressure case of 380 torr of argon to determine which type of mode discussed previously is dominant. Figure 4 shows the real and imaginary parts of the complex eigenvalue for the case of 380 torr
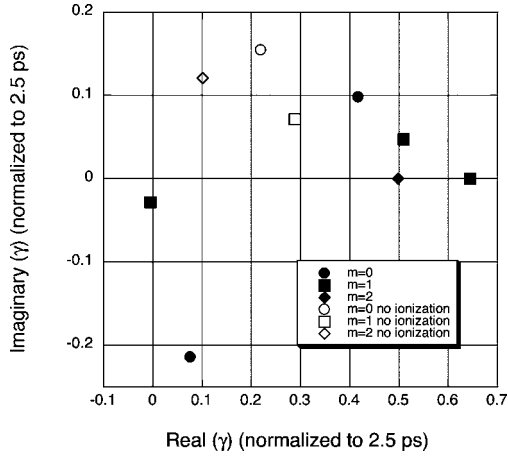
FIG. 4. Location of the complex growth, γ, during a 2.5 ps interval, obtained by solving Eq. (9) at one particular time, 88 ps. Solutions to Eq. (9) without ionization effects are included to emphasize the importance of the ionization process on the modes with no frequency shift $\text{Im}(\gamma) \cong 0$. Several modes have been identified depending on the azimuthal mode number, m, and on the initial search parameters.

of argon. Shown are normalized growth rates, γdt, where $dt = 2.5$ ps, for three different azimuthal mode numbers $m = 0$, 1, and 2, and for each m value there are several modes that are distinguished by their radial profile. In this figure, and subsequent figures, the scattered wave number k_s was chosen to correspond to the wave number that maximized total (time integrated) growth for the parameters under consideration, and this will be discussed subsequently. The eigenvalues and scattered mode solutions were determined using a shooting method to integrate Eq. (9) by starting from $r_{\max}$ where the solution matched an outward propagating wave; $H_m^{(1)}(\kappa r_{\max})$, where $H_m^{(1)}$ is an mth order Hankel function of first kind. Here $r_{\max}$ is taken to be well outside the plasma region. We then searched for an eigenvalue such that the solution was regular at the origin, $r = 0$, e.g., $du_s/dr = 0$ for $m = 0$ or $u_s = 0$ for $m \neq 0$. Several different modes were identified, depending on the initial guess for the eigenvalue in the search routine. We have also included as open symbols solutions for the case where the ionization effects in Eq. (9) have been removed, specifically, $\nu_I = 0$. These solutions, with no ionization effects, have lower growth rate, and all contain nonzero frequency shifts. The importance of this last point will be emphasized later.

Notice that the largest growth rate occurs for an $m = 1$ mode with virtually zero frequency shift. There is also an $m = 1$ mode with slightly lower growth rate and a larger real frequency, as well as what appears to be a marginally stable $m = 1$ mode. Figure 5 shows radial profiles for each of the growing modes as well as the real part of the equivalent potential, $Q(r)/M(r)$ in Eq. (9). In the case of the highest growth mode, Fig. 5(a), we see a pole of the potential is near the real-r axis at approximately $r = 3$ μm. This pole is associated with a singular point, $M = 0$, in Eq. (9) and is primarily determined by the ionization, $\gamma \approx (2 - \eta)\nu_I(r)$. The derivative of the scattered field changes abruptly near the pole as is expected for the solution near the singular point. The mode
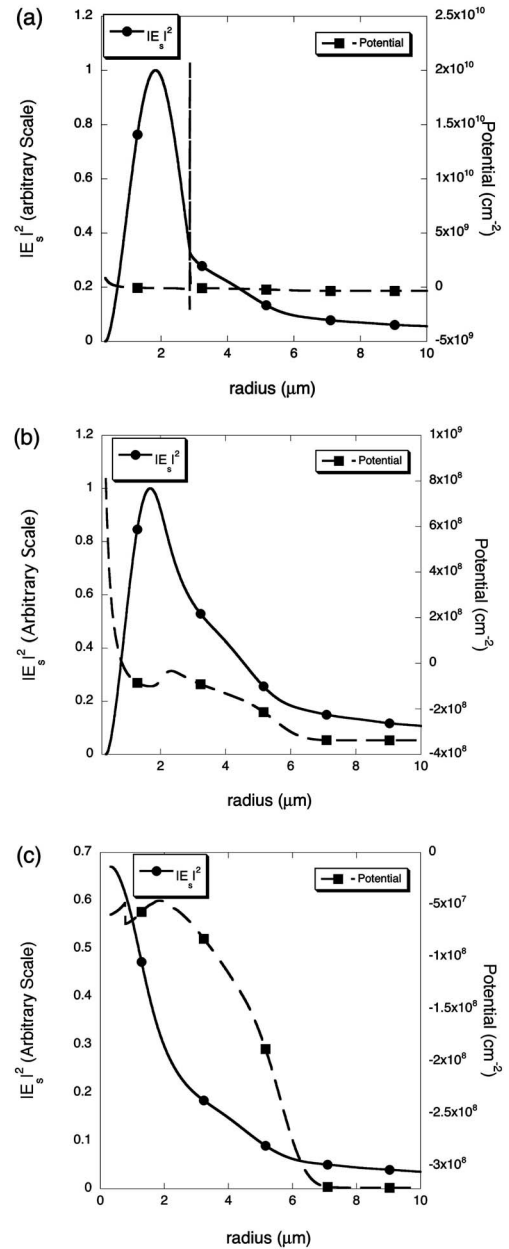
FIG. 5. Solution functions for Eq. (9) for two of the $m = 1$ modes depicted in Fig. 4. Both the scattered mode $|u_s|^2$ and the real part of the potential function, Q/M, are shown. (a) corresponds to the mode that has negligible frequency shift and a growth of approximately 0.65. (b) corresponds to the mode with positive frequency shift and a growth of approximately 0.5. (c) corresponds to the $m = 0$ mode at this time that is associated with the positive frequency shift and growth of approximately 0.4. Notice in (a) that the potential function has a complex pole near the real axis. This pole corresponds to a singular point in Eq. (9) when $M(r) = 0$. This local singular point appears to dominate the dynamics when this singular point can be found.

profile and equivalent potential for the lower growth rate $m = 1$ mode of Fig. 4 is shown in Fig. 5(b). This mode has a greater radial extent than the highest growth mode. There appears to be a slight well in the effective potential near 2 μm that contains the mode. In contrast to the high growth
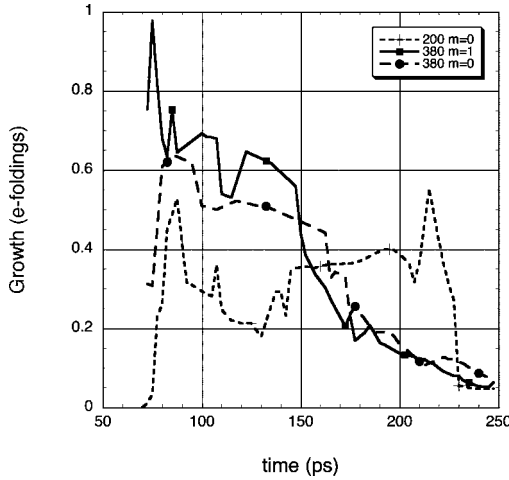
FIG. 6. Instantaneous growth versus time during pulse for both the 200 torr case and the 380 torr ($m=0$ and $m=1$ mode). Notice the 380 torr cases have significant growth in the early part of the pulse, while the 200 torr case has most of the growth after the center of the pulse has passed, at 120 ps. This timing can be understood in terms of the dominant mechanism, ionization in the high-pressure case and mode coupling in the low-pressure case.

rate mode, this mode is not associated with a singularity in Eq. (9). We have also included the radial mode profile and potential for the case with $m=0$. Here there is a well-defined channel in the potential about $r=0$, which serves to contain the guided mode.

Figure 6 shows the incremental growth γdt, where $dt = 2.5$ ps, as a function of time during the channel development for two different pressures, 200 and 380 torr of argon. The fastest growing mode for 200 torr argon has $m=0$ while for 380 torr the fastest growing mode has $m=1$. We also include in this figure the $m=0$ mode for 380 torr. The maximum growth rates appear to occasionally jump with time. We believe that this is a consequence of our numerical solutions of Eq. (9) and our procedure for finding roots. In particular for the $m=1$ modes, the modes that we seek have singularities close to the real-r axis, making them sensitive to the numerical grid. Further, we generate new profiles only every 2.5 ps, and sometimes it is difficult to follow a root from one time step to the next.

It is apparent from this figure that for the high-pressure case the majority of the growth occurs early in the channel evolution. This is in contrast to the low-pressure case in which most growth occurs toward the end of the simulation. This timing can be understood in terms of the dominant mechanism for the unstable growth. For the $m=1$ mode in the high-pressure case, the early growth is dominated by ionization physics and modes are of the type shown in Fig. 5(a). To confirm this hypothesis we examined the mode for the fastest growing period. Figure 7(a) shows the field $|E_s|^2$ and the potential $Q(r)/M(r)$ for the fastest growing mode during the pulse in the 380 torr case. This mode occurs at 75 ps, as seen in Fig. 6, prior to the plasma channel formation at approximately 90 ps. This mode is clearly centered on the pole in the effective potential. This mode is due to the singular point in Eq. (9) and is dominated by the ionization rate. For
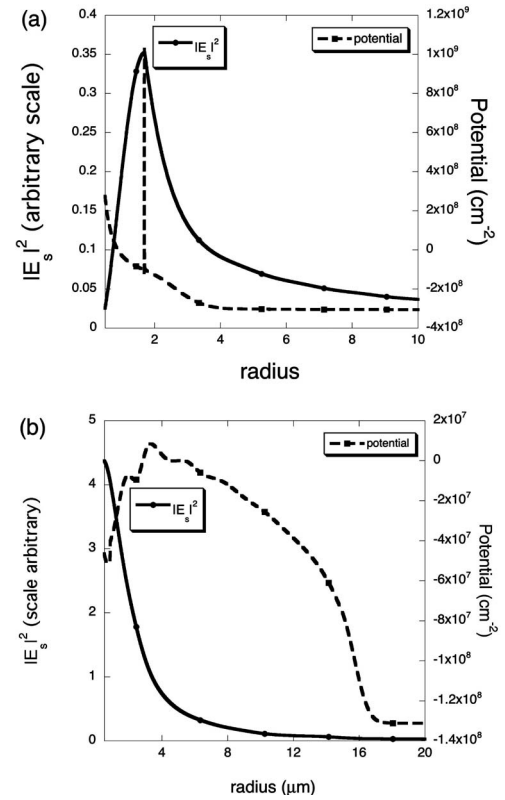
FIG. 7. (a) Scattered field $|E_s|^2$ and potential function Q/M at the fastest growing point during the calculation. This mode occurs before the plasma channel has been formed due to electron density inversion, which happens at approximately 90 ps. This mode is clearly centered on the local singular point of the equation. This singular point is driven by the ionization rate and corresponds to an ionization mode. (b) Scattered wave $|E_s|^2$ and potential function Q/M for the low-pressure case, 200 torr. The scattered field is localized in the plasma channel with significant enhancement relative to the outward propagating field in the outer radius.

the 380 torr case the singular point in Eq. (9) continues to dominate the dynamics until approximately 150 ps. After this time the growth associated with this ionization mode is less than the growth associated with the global solution within the channel region. This change in behavior is apparent from the kink in the growth curve at 150 ps. For the $m=0$ mode plotted in Fig. 5(c), the mode structure appears to be controlled by channel confinement rather than ionization physics. However, it is apparent from Fig. 4 that there is still an important effect of ionization on the scattered modes, since the growth rates calculated with ionization included are larger than those with no ionization present. For the high-pressure case the axicon field is excluded from the central channel by the plasma at later times. Thus, the majority of the growth at high pressures occurs early in the channel evolution compared with the low-pressure case.

The ionization mechanism is also active at very early times for the low-pressure case, e.g., before the channel forms and a well-defined resonant mode exists, prior to 100 ps. However, as the channel evolves for the low-pressure case the growth associated with the singular point due to ionization decreases and the coupling to quasi-guided modes
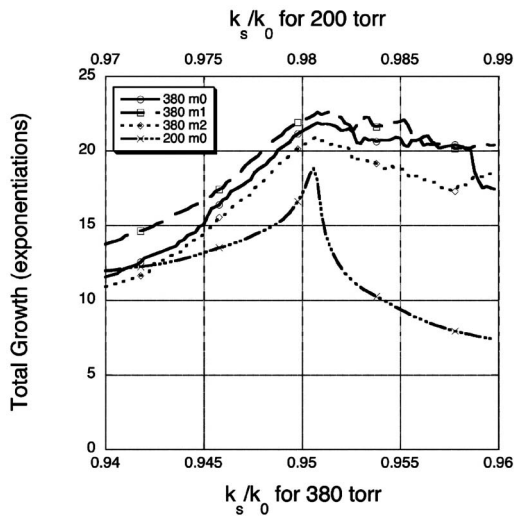
FIG. 8. Total instability growth for $m=0,1,2$ for 380 torr argon and $m=0$ for 200 torr argon. The 380 torr cases are referenced to the lower axis and the 200 torr case refers to the upper x axis. The location of the maximum growth corresponds roughly to the scattered wave number predicted using the linear theory. However, for the high-pressure case there is little resonance since the local dispersion created by the ionization process dominates. For the low-pressure case there is more resonant behavior; however, the growth in this mode is less pronounced.

begins to dominate. This situation can be seen in Fig. 7(b), which presents results from the lower pressure calculation, 200 torr argon at 175 ps. Notice that $|E_s|^2$ is localized on axis in the potential well formed by the plasma channel. For this type of mode the analysis leading to Eq. (14) is expected to be valid. Here there is an enhancement at the scattered mode wave number $k_s > k_a$. This mode is a global mode, which depends on the solution to Eq. (9) rather then a local ionization mode at a singular point of the equation. This type of mode is not as prevalent in the high-pressure case, where the axicon field is excluded from the axis as shown in Fig. 3.

We have repeated this numerical calculation for a wide range of pressures and scattered modes wave numbers. Figure 8 presents a comparison of the total growth of the most unstable mode for the case of 380 torr argon with $m=0$, 1, and 2 and 200 torr argon $m=0$ for many values of scattered wave number. Notice that for the 200 torr case, the growth has a sharp peak at the resonant wave number $k_s=k_g$. For the 380 torr case the growth is less localized in scattered wave number. This observation is consistent with the discussion presented above since the low-pressure case is dominated by a channel confinement, while the high-pressure case includes modes dominated by local ionization effects. However, there is still a scattered mode that maximizes growth even in the high-pressure case.

Figure 9 shows the experimental modulation wave number versus gas pressure for several pressures. Also in Fig. 9 are the modulation wave numbers corresponding to the calculated modes with the largest total growth. The calculated modulation wave numbers agree well with experiment including the rapid change as a function of pressure. Figure 10 compares the cumulative growth for the most unstable mode
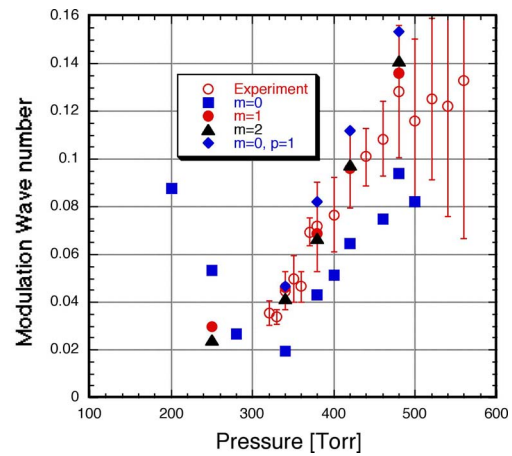
FIG. 9. (Color online) Modulation wave number, in μm^{-1}, versus pressure: the open circles are the measured data along with error bars, the solid symbols are the calculated values for different modes of the channel.

for 380, $m=1$ ($m=0$) and 200 torr. The 380 torr case has six (four) more exponentiations than the 200 torr case. Thus the high-pressure case is more unstable to this modulation instability than the low-pressure case. Further, the high-pressure case has significant growth by the middle of the simulation, 15 (13) exponentiations by 120 ps. The 200 torr case has approximately six exponentiations by the middle of the simulation. Thus, we would expect enhanced coupling of the scattered mode to the plasma channel in the 380 torr case compared to the values obtained, whereas for the 200 torr case, the model calculation is likely valid over the duration of the simulation since significant mode growth, e.g., 15 exponentiations, does not occur until near the end of the simulation, 200 ps.
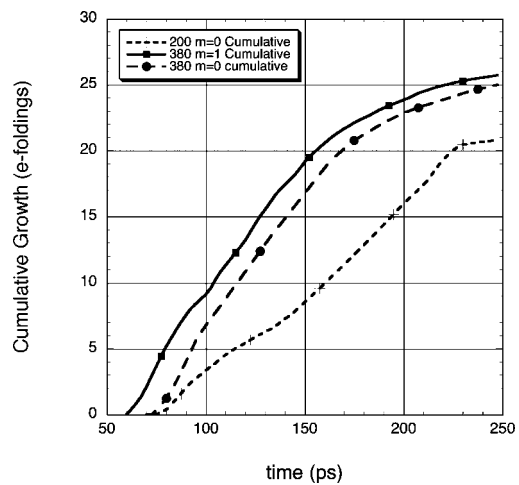
FIG. 10. Cumulative growth of the unstable mode for both the 200 torr, $m=0$ mode and the 380 torr, $m=0$ and $m=1$ mode. Notice that by the middle of the laser pulse, 120 ps, the high 380 torr modes have nearly 15 exponentiations while the 200 torr mode does not achieve this milestone until nearly 200 ps, near the end of the pulse.

IV. HIGH THERMAL CONDUCTIVITY LIMIT

The preceding analysis was carried out in the limit that electron thermal conduction was negligible. However, during the channel evolution, particularly early when the electron temperature is high and the channel radius is small, heat conduction is likely to be important. This limitation in the previous analysis is particularly relevant to modes with azimuthal mode $m \neq 0$, since in this case thermal conduction will eliminate any temperature variation across the plasma channel. For $m = 0$ modes, temperature fluctuations can still be maintained due to the large barrier to thermal conduction at the channel edge, apparent in Fig. 2(b). Therefore, the previous analysis is still expected to describe the $m = 0$ modes.

Electron thermal conduction is included in the hydrocode results that give rise to the profiles in Figs. 2(a)–2(c). The coefficient of thermal conduction used is given by the Spitzer value. When the electron mean free path exceeds the gradient scale length a thermal flux limit is imposed. Such a scheme is difficult to linearize, and this is one reason thermal conduction was ignored in our initial studies. To examine the effect of high electron thermal conductivity we will present a modified model where the thermal relaxation rate is taken to be large compared to the instability growth rate.

We begin by modifying Eq. (5c) to include thermal conduction,

$$\frac{3}{2}\frac{\partial}{\partial t}\widetilde{p} - n_0 D_{\parallel}^e \nabla^2 \widetilde{T}_e = \frac{n_0 e^2}{m_e}\frac{\nu}{\nu^2 + \omega^2}\widetilde{E}_s(r,t)E_a^*, \quad (17)$$

where, for simplicity, we have ignored gradients in the equilibrium density and thermal diffusivity, $D_{\parallel}^e = 3.2\tau_e T_e/m_e$, and $\tau_e = 3.44 \times 10^5 T_e^{3/2}/(n\Lambda)$ is the electron collision time. When thermal conductivity is large, temperature perturbations will be suppressed. Thus, we must modify the source terms in Eq. (5a):

$$\frac{\partial}{\partial t}\widetilde{n} + \boldsymbol{\nabla}\cdot\widetilde{\nu}n_0 = 2n_0\widetilde{n}S(T_e) + n_0(\widetilde{n}_s T_a^* + n_a^*\widetilde{T}_s)\frac{\partial S}{\partial T_e}. \quad (18)$$

This modification has the effect of changing the quantity Δ that appears in Eq. (7), which now becomes $\Delta' = 1 - 2\nu_I/\gamma$. Further, the modification eliminates the term proportional to γ_I^2 in Eq. (6).

The perturbed pressure given by Eq. (17) enters Eq. (6) for the perturbed density through terms proportional to γ_0^3/γ^3. With the addition of thermal conduction, one of the γ's in the denominator must be replaced as follows: $1/\gamma \rightarrow [\gamma - (2/3)D_{\parallel}^e\nabla_{\perp}^2]^{-1}$. Thus, the perturbed density is now given by

$$\frac{\hat{n}}{n_0} = \frac{c^2}{\omega_p^2\Delta'}\left[\nabla_{\perp}^2\left(\gamma - \frac{2}{3}D_{\parallel}^e\nabla_{\perp}^2\right)^{-1}\frac{\gamma_0^3}{\gamma^3}u_s u_a^* + \boldsymbol{\nabla}_{\perp}\cdot\left(\frac{\gamma_p^2}{\gamma^2}\boldsymbol{\nabla}_{\perp}u_s u_a^*\right)\right.$$
$$\left. + \frac{\omega_p^2}{c^2}\left(\frac{\gamma_s}{\gamma}\right)u_s u_a^*\right].$$

In the limit of high electron thermal conductivity we can assume $\gamma \ll D_{\parallel}^e\nabla_{\perp}^2$. Thus the expression for the perturbed

density simplifies and the new equation, to replace Eq. (8), for the scattered wave becomes

$$\left(\nabla_{\perp}^2 + 2i\frac{\omega_0}{c^2}\gamma + \kappa^2(r,\omega_0,k_s)\right)u_s$$
$$= \frac{u_a}{\Delta'}\left[-\frac{3}{2D_{\parallel}^e}\left(\frac{\gamma_0^3}{\gamma^2}u_s u_a^*\right) + \boldsymbol{\nabla}_{\perp}\cdot\left(\frac{\gamma_p^2}{\gamma^2}\boldsymbol{\nabla}_{\perp}u_s u_a^*\right)\right.$$
$$\left. + \frac{\omega_p^2}{c^2}\left(\frac{\gamma_s}{\gamma}\right)u_s u_a^*\right]. \quad (19)$$

In the same way we analyzed Eq. (8) in terms of a quasi-guided mode, we can examine the solutions of Eq. (19) with high thermal conductivity. This process yields modified coefficients for Eq. (14) with, $A = 0$,

$$B = \frac{\frac{1}{k_0^2}\left[\int 2\pi r dr\left(u_a u_g^*\boldsymbol{\nabla}_{\perp}\cdot\gamma_p^2\boldsymbol{\nabla}_{\perp}u_g u_a^* - \frac{3}{2D_{\parallel}^e}\gamma_0^3|u_a|^2|u_g|^2\right)\right]}{\int 2\pi r dr|u_g|^2},$$

and $C = C$.

The dispersion relation in this case becomes

$$D(\gamma,\delta k) = \gamma^2 + \frac{i\,\text{sgn}(B)\Gamma^2}{1 + i\delta k/k_d} = 0$$

with $\Gamma^2 = [|B|k_0/2k_d]$. This dispersion relation will in general yield one stable and one unstable mode with the growth rate dependent on Γ. Notice that in this case B depends on both the ponderomotive force and heating rate. With $\gamma_p^2 = \gamma_0^3/3\nu$ we find that the ratio of the two terms in B varies as the laser radiation scale size r_m^2 divided by the electron thermal mean free path λ_{mfp}^2, i.e., r_m^2/λ_{mfp}^2. For the parameters that apply early in the channel evolution, this ratio is of order unity, implying that the contribution from the ponderomotive force is comparable to the contribution from Joule heating. This is in contrast to the low thermal conductivity case where the growth was dominated by Joule heating.

We now turn to numerical solutions to Eq. (19) to determine $\gamma(k_s)$, again with boundary conditions outside the plasma requiring the scattered field to match to $H_m^{(1)}(k_s r)$ and requiring the solution is regular at $r = 0$. Figure 11 shows the scattered field for conditions comparable to those giving rise to the scattered field in Fig. 5. In Fig. 12, we show the calculated total growth, $\Gamma = \int \gamma(k_s)dt$, for a range of scattered wave numbers k_s. Notice that although the system is still unstable, the growth in the high thermal conductivity limit is reduced, as expected. Also notice that the dependence on axial wave number is less significant than in the case of no thermal conductivity with the dominant mode coinciding with the axicon field. Therefore, the modulation period would be infinite, as is the case for resonant coupling, Ref. [9]. Therefore, the overall effect of thermal conductivity may be to reduce the $m > 0$ modes and lead to an instability dominated by the $m = 0$ modes.

V. CONCLUSIONS

We have presented experimental evidence of an instability in the generation of plasma channels using axicon field
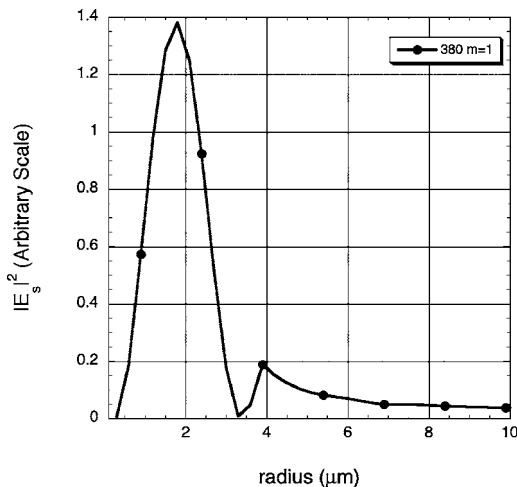
FIG. 11. $m=1$ scattered field mode structure at 88 ps in the case of high thermal conductivity.

FIG. 12. The cumulative growth for the $m=1$, 2, and 3 modes in the case of high thermal conduction. Notice that the overall growth is greatly reduced from the case where thermal conduction was neglected (Fig. 8). Also notice that the fastest growing modes coincide with the axicon field wave number, thus leading to an infinite modulation period.

breakdown at moderate gas pressures and pulse duration. We have described a model to describe this instability and shown that the instability is parametric in nature. This instability is associated with the nonlinear coupling of a scattered mode to the incident axicon field through ionization, heating, and ponderomotive physics. We examine solutions to this model in two limiting conditions, for negligible and for high electron thermal conductivity. We expect the actual solutions to lie somewhere between these limiting cases. However, since the $m=0$ modes are not as affected by thermal conduction, we expect the unstable growth to be attributable to $m=0$ modes. We show that this model accurately predicts the unstable scattered wave number and accounts for the strong pressure dependence of the instability wavelength.

The onset of this instability may preclude use of axicon formed plasma channels for pressures above the resonant coupling pressure. However, it might be possible to design plasma channels to provide efficient coupling to either high harmonics or predetermined wave number by allowing tight control of axially periodic structures in plasma channels.

ACKNOWLEDGMENTS

[1] H. M. Milchberg, C. G. Durfee III, and T. J. McIlrath, Phys. Rev. Lett. **75**, 2494 (1995); H. M. Milchberg, C. G. Durfee, and J. Lynch, J. Opt. Soc. Am. B **12**, 731 (1995).

[2] P. Sprangle, B. Hafizi, J. R. Penano, R. F. Hubbard, A. Ting, A. Zigler, and T. M. Antonsen, Phys. Rev. Lett. **85**, 5110 (2000); H. M. Milchberg, T. R. Clark, C. G. Durfee, T. M. Antonsen, and P. Mora, Phys. Plasmas **3**, 2149 (1996).

[3] C. G. Durfee III and H. M. Milchberg, Phys. Rev. Lett. **71**, 2409 (1993); C. G. Durfee III, J. Lynch, and H. M. Milchberg, Phys. Rev. E **51**, 2368 (1995).

[4] P. Volfbeyn, E. Esarey, and W. P. Leemans, Phys. Plasmas **6**, 2269 (1999).

[5] E. W. Gaul, S. P. Le Blanc, A. R. Rundquist, R. Zgadzaj, H. Langhoff, and M. C. Downer, Appl. Phys. Lett. **77**, 4112 (2000).

[6] A. Zigler, Y. Ehrlich, C. Cohen, J. Krall, and P. Sprangle, J. Opt. Soc. Am. B **13**, 68 (1996).

[7] T. R. Clark and H. M. Milchberg, Phys. Rev. Lett. **78**, 2373 (1997).

[8] T. R. Clark and H. M. Milchberg, Phys. Rev. Lett. **81**, 357

(1998); T. R. Clark and H. M. Milchberg, Phys. Rev. E **61**, 1954 (2000).

[9] J. Fan, E. Parra, and H. M. Milchberg, Phys. Rev. Lett. **84**, 3085 (2000); J. Fan, E. Parra, K. Y. Kim, I. Alexeev, H. M. Milchberg, J. Cooley, and T. M. Antonsen, Phys. Rev. E **65**(5), 056408 (2002).

[10] S. S. Bychkov, S. V. Gorlov, A. V. Makarov, L. Ya. Margolin, L. N. Pyatnitskii, and A. D. Tal'virskii, Quantum Electron. **29**(3), 243 (1999).

[11] L. Ya. Margolin, Quantum Electron. **29**(3), 246 (1999).

[12] L. N. Pyatnitskii, Plasma Phys. Rep. **27**, 799 (2001); Y. Ping, I. Geltner, and S. Suckewer, Phys. Plasmas **8**(9), 4174 (2001).

[13] R. W. P. McWhirter, in *Plasma Diagnostic Techniques*, edited by R. H. Huddlestone and S. L. Leonard (Academic Press, New York, 1965).

[14] D. Pesme, W. Rozmus, V. T. Tikhonchuk, A. Maximov, I. Ourdev, and C. H. Still, Phys. Rev. Lett. **84**, 278 (2000).

[15] *Basic Plasma Physics I*, edited by A. A. Galeev and R. N. Sudan (North-Holland Publishing Company, Amsterdam, 1983), Chap. 3.2, p. 452.